Biochimica et Biophysica Acta 1837 (2014) 1821–1834

Contents lists available at ScienceDirect

Biochimica et Biophysica Acta

journal homepage: www.elsevier.com/locate/bbabio

Photo-oxidation of tyrosine in a bio-engineered bacterioferritin 'reaction centre'—A protein model for artificial photosynthesis ☆

Kastoori Hingorani [a,*], Ron Pace [b,*], Spencer Whitney [a], James W. Murray [c], Paul Smith [b], Mun Hon Cheah [a], Tom Wydrzynski [a], Warwick Hillier [a]

[a] Building 134, Linnaeus Way, Research School of Biology, The Australian National University, ACT 0200, Australia
[b] Building 137, Sullivans Creek Road, Research School of Chemistry, The Australian National University, ACT 0200, Australia
[c] 724 Sir Ernst Chain Building, South Kensington Campus, Division of Molecular Biosciences, Imperial College London, London SW7 2AZ, United Kingdom

ARTICLE INFO

Article history:
Received 14 April 2014
Received in revised form 11 July 2014
Accepted 29 July 2014
Available online 5 August 2014

Keywords:
Artificial photosynthesis
Protein engineering
Electron transfer
Tyrosine oxidation
Photosystem II
Bacterioferritin

ABSTRACT

The photosynthetic reaction centre (RC) is central to the conversion of solar energy into chemical energy and is a model for bio-mimetic engineering approaches to this end. We describe bio-engineering of a Photosystem II (PSII) RC inspired peptide model, building on our earlier studies. A *non-photosynthetic* haem containing bacterioferritin (BFR) from *Escherichia coli* that expresses as a homodimer was used as a protein scaffold, incorporating redox-active cofactors mimicking those of PSII. Desirable properties include: a di-nuclear metal binding site which provides ligands for bivalent metals, a hydrophobic pocket at the dimer interface which can bind a photosensitive porphyrin and presence of tyrosine residues proximal to the bound cofactors, which can be utilised as efficient electron-tunnelling intermediates.

Light-induced electron transfer from proximal tyrosine residues to the photo-oxidised $ZnCe_6^{\bullet+}$, in the modified BFR reconstituted with both $ZnCe_6$ and Mn^{II}, is presented. Three site-specific tyrosine variants (Y25F, Y58F and Y45F) were made to localise the redox-active tyrosine in the engineered system. The results indicate that: presence of bound Mn^{II} is necessary to observe tyrosine oxidation in all BFR variants; Y45 the most important tyrosine as an immediate electron donor to the oxidised $ZnCe_6^{\bullet+}$ and that Y25 and Y58 are both redox-active in this system, but appear to function interchangebaly. High-resolution (2.1 Å) crystal structures of the tyrosine variants show that there are no mutation-induced effects on the overall 3-D structure of the protein. Small effects are observed in the Y45F variant. Here, the BFR-RC represents a protein model for artificial photosynthesis.

1. Introduction

Photosynthetic organisms (plants, algae and cyanobacteria) are nature's own sophisticated solar panels and carbon sequestering systems. Oxygenic photosynthesis, a process that converts solar energy into chemical energy today sustains a broad variety of complex higher life forms on this planet, through oxygen evolution and carbon fixation. The component regarded as the 'engine-room' of this process is the Photosystem II (PSII) reaction centre (RC). The RC chemically drives unfavourable reactions, by extracting energy from photons [1,2]. All natural reaction centres function in essentially the same way, with only minor variations in their cofactors. Minimally, a reaction centre holds a photoactive pigment (P) and an acceptor molecule (A). Upon illumination, the excited state P^* can interact with a nearby acceptor and undergo electron transfer to form a charge-separated state (P^+/A^-) [1]. The molecular organisation of a reaction centre is essentially a series of transmembrane protein regions that localise the P^+/A^- pair to span the membrane. The core structure of all reaction centres is C_2 symmetric and in some systems the symmetry leads to bifurcated electron transfer pathways [1].

To assemble artificial reaction centres on protein scaffolds, the two minimal requirements are (i) selection and incorporation of pigments/chromophores for light capture, that initiate photochemistry and (ii) the choice and placement of redox-active intermediates for electron transfer. Electron donors and acceptors perform primary charge separation and their properties underpin the efficiency of the system. Detailed principles determining design and engineering of light capture and electron transfer processes between electron donor and acceptor molecules through redox-active intermediates in both natural and *de novo* protein scaffolds have been discussed previously; see [3–5].

We have used *Escherichia coli* bacterioferritin (BFR) as a protein scaffold to introduce key redox active intermediates in a PSII reaction

☆ This paper is dedicated to the memory of Warwick Hillier, who saw this work to completion, however tragically passed away after protracted illness, just prior to the submission of this paper. He was a dear friend and colleague to us all, who will miss him dearly, as will we feel the broader science community.

* Corresponding authors.
E-mail addresses: kastoori.hingorani@anu.edu.au (K. Hingorani), ron.pace@anu.edu.au (R. Pace).

http://dx.doi.org/10.1016/j.bbabio.2014.07.019
0005-2728/

centre inspired *in vitro* model system [4,6]. BFR is a soluble non-toxic iron storage and detoxification protein [7,8] that assembles into a dodecamer (24-subunit) with a hollow sphere of ~8 nm internal diameter (Fig. 1a). The BFR monomeric subunit is a four helix bundle (~18.5 kDa), where the four helices align anti-parallel to each other with a small fifth helix at the C-terminus, which aligns almost perpendicular to the rest of the bundle (Fig. 1b) [9,10]. Each of the four-helix bundles contains a di-nuclear metal binding site that binds two Fe^{II} atoms with histidine (H54 and H130) and glutamate (E51, E18, E127 and E94) residues as capping ligands. The two atoms are connected by the two bridging carboxylate groups (E51 and E127) (Fig. 2a). Single methionine residues, one from each monomer, provide a pair of axial ligands to the metal centre of iron-protoporphyrin IX (haem group) in the assembled BFR homodimer (Fig. 2b).This haem binding site at the dimer interface of the two four helix bundles is hydrophobic [9].

The BFR homodimer was used to reverse engineer PSII RC reactions, providing a novel way to explore the complex pathways of light-driven electron transfer in an artificial PSII analogue system. Extending from our earlier work [6,11], we here demonstrate (i) binding of $Mn^{II,II}$ at the di-nuclear metal binding site, (ii) binding of a photoactive pigment ($ZnCe_6$) at the hydrophobic pocket of the protein, by replacing the intrinsic haem group [12] and (iii) photo-oxidation and localisation of tyrosine residue (s) in the engineered BFR system.

In previous work, light-induced experiments in the modified BFR suggested that, upon photo-activation of the bound $ZnCe_6$, the weakly coupled $Mn_2^{II,II}$ at the di-nuclear site is oxidised and a ~ 25 G wide EPR spectrum centred at $g = 2.0058$ is observed [6]. This ~25 G wide spectrum was assigned to a tyrosine radical because of its line shape and the absence of quinone electron acceptors as possible contributing radicals [13,14]. The source of this spectrum was not established.

There are seven tyrosine residues per BFR monomer and therefore fourteen possible tyrosine residues per homodimer that might be redox-active. The three BFR tyrosine residues Y25, Y58 and Y45, which are within electron tunnelling distance from both the photoactive pigment and the metal centre, were sequentially mutated to phenylalanine (Fig. 3). Tyrosine 25 which is 4.3 Å from the nearest metal is highly conserved amongst other ferritins and bacterioferritins [15]. It is also hydrogen bonded to Glu 94, which is one of the metal ligands. Tyrosine 58 is unique to *E. coli* BFR in its position and is commonly replaced by a leucine or a phenylalanine residue in other ferritins. Tyrosine 45 provides van der Waals contact to the haem within the hydrophobic pocket at a distance of 3.1 Å [9].

Site-directed mutagenesis of tyrosine to phenylalanine has previously been used to identify the tyrosine radicals $Y_D^{\bullet}$ and $Y_Z^{\bullet}$ in PSII [13,16–18]. Here, we have constructed three tyrosine variants of the engineered BFR, resolved their crystal structures (~2.1 Å) and present a highly probable photo-oxidation electron transfer pathway within the fully assembled (all cofactors bound) BFR reaction centre.

2. Materials and methods

2.1. Molecular methods

In this study BFR^1 was used as the control. BFR^1 is a double mutant of the wild type *E. coli* BFR with two external histidine residues replaced by arginine residues (H46R and H112R) [6,11]. This is because, in other studies, spontaneous ligation of $ZnCe_6$ to histidine residues in both *de novo* peptides and to cytochrome b562 has been reported [19,20]. The three tyrosine variants (Y25F, Y45F and Y58F) were generated using the *bfr*^{1} gene (cloned in pET30 Xa/LIC vector) as the template. This was done using the Quick Change Site Directed Mutagenesis Kit (Strategene). All genes were sub-cloned in frame with a N-terminal 6 x histidine tagged ubiquitin sequence (H_6 -Ub), in a fusion *E. coli* expression system pHUE vector for protein expression [21,22]. The sub-cloning of the relevant genes was a two-step process. First, all genes were PCR amplified to introduce a 5′- *Sac*II and a 3′- *Hind*III cloning site and cloned into pGEM®-Teasy cloning vector (Promega) by TA cloning. The PCR primers used were *Sac*II 5′-TCCGCGGTGGAGATATGAA AGGTGATACTAAAG-3′ and *Hind*III 5′-AGATCCGCGAAGAAGGTTAAGCTT-3′. Correctly transformed plasmids were identified by blue–white selection. Second, sequenced mutant *bfr*^{1} genes were cloned into the *Sac*II-*Hind*III cut pHUE using standard ligation protocols.

2.2. Protein expression and purification

BFR^1 and the tyrosine variants were over-expressed in *E. coli* BL21 (DE3) cell line, where protein expression was induced using 1 mM isopropyl-β-D thiogalactopyranoside (IPTG). The recombinant his-tagged protein (H_6-Ub-BFR) was purified using Immobilised Metal Affinity Chromatography (IMAC)-nickel-sepharose chromatography

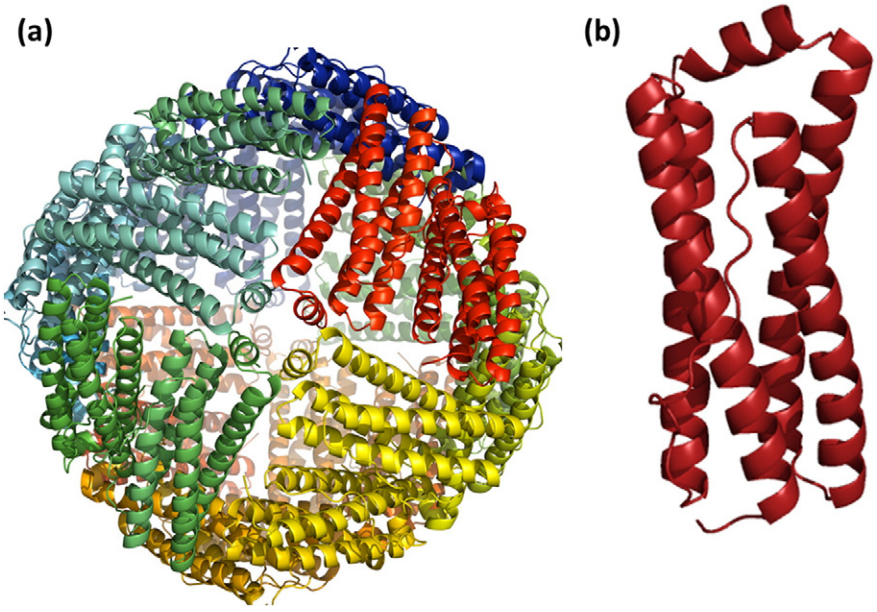

Fig. 1. Cartoon diagram of *E. coli* bacterioferritin (BFR). (a) Spherical, dodecameric (24-subunit) form of BFR; (b) monomeric subunit (four-helix bundle) of BFR (PDB file: 1BCF). Figure taken from Hingorani and Hillier 2012 [4].

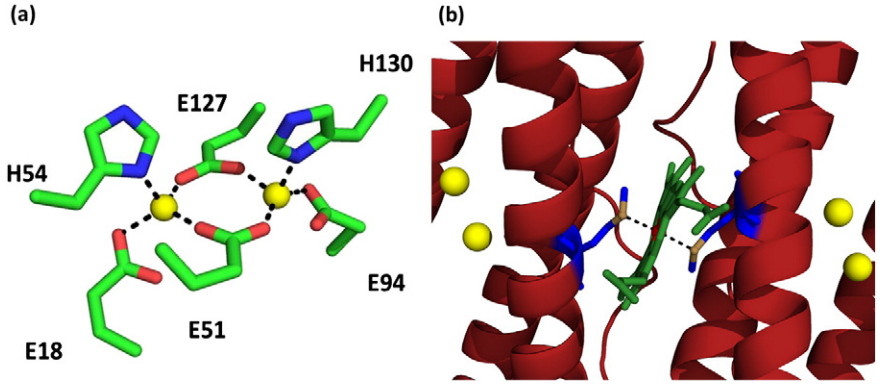

Fig. 2. Cartoon of cofactor binding sites in *E.coli* BFR. (a) Di-nuclear metal centre; metal ($Mn^{II, II}$) shown as sphere(yellow) in its ligand environment, residues (colour coded by atom type) that provide direct ligands shown as a dotted line (black); (b) haem-binding site at the hydrophobic interface shown as a bi-axial ligation at equivalent M52 (blue) in each subunit (PDB file: 1BCF). Figure adapted from Hingorani and Hillier 2012 [4].

column (AKTA prime, GE Healthcare). The his-tag (H_6-Ub) at the N-terminus of the purified protein was cleaved using a ubiquitin specific protease (H_6-Usp-2) as described in [22]. IMAC- nickel affinity was repeated to remove the contaminating H_6-Usp-2 and H_6-Ub peptides, where the non-binding BFR variant protein(s) were eluted. The purified protein was of single band purity on SDS-gel electrophoresis and was stored in TBS storage buffer (25 mM Tricine, 137 mM NaCl, 2.7 mM KCl; pH 7.5; 20% (*v*/*v*) glycerol). The protein samples were prepared in TBS buffer (-glycerol) for all analytical experiments unless otherwise stated.

2.3. Chemical methods

The haem bound to the genetically modified BFR[1] protein and the tyrosine variants was removed using a method adopted from [12]. Non-haem iron bound to the protein was removed by exhaustive dialysis in the presence of DTT and EDTA [23]. The total Fe^{II} content of the DTT/EDTA treated protein samples was determined using analytical inductively-coupled-plasma mass spectrometry (ICP-MS).[1] The ICP-MS results established that for all samples, there was less than 0.04 moles of Fe^{II} per mole of apo-BFR present before cofactor assembly. Protein concentrations for the apo-protein were determined using an ε280 nm value of 20,340 M^{-1} cm^{-1} (ExPASy, online bioinformatics resource portal). A 2 mM stock of $ZnCe_6$ was prepared by adding 1:1 molar equivalents of ZnAcetate and Ce_6 both made in glycine buffered saline [19,24]. Immediately after mixing, the reaction was degassed under vacuum for 15 min. All $ZnCe_6$ solutions were made in vacuum seal glass vials in the dark and stored at 4 °C (dark). The incorporation of Zn into the Ce_6 porphyrin was determined by monitoring the shift in the Soret and Q_y bands of the absorption spectra of the metalloporphyrin $ZnCe_6$ using UV–visible spectroscopy. The Soret band of $ZnCe_6$ compared to that of Ce_6 shows about a 10 nm red-shift (401 → 412 nm) in the visible spectrum and about a 20 nm blue-shift (654 → 633 nm) in the Q_y region. The $ZnCe_6$ was added to the apo-BFR in stoichiometric amounts. Successful binding of $ZnCe_6$ to BFR variants was also determined by monitoring the shifts in the Soret and Q_y region of the visible spectra [19,24]. UV–Vis spectroscopy was carried out on a Cary 300 Spectrometer (Varian, USA).

2.4. X-ray crystallography

Crystal structures of apo-BFR[1] and variants were determined. Samples were concentrated to around 10 mg/ml and were screened for crystallisation against the JCSG + screen [25], using sitting-drop vapour diffusion, with plates prepared using a Mosquito® robot (ttplabtech, USA). Crystals appeared in numerous screen conditions and in several crystal forms and were mounted for structure determination. Each crystal was cryoprotected for a few minutes in the mother liquor solution with 30% (*v*/*v*) glycerol added, and then mounted in a loop and flash-cooled in liquid nitrogen for transport to the synchrotron. Diffraction data were collected on beamline I04 at Diamond Light Source. Data were integrated and scaled using XDS [26] and programmes of the CCP4 [CCP41994] suite, used through the xia2 pipeline [27]. The structures were then solved by molecular replacement with PHASER [28] using the *E. coli* bacterioferritin structure (PDB: 2VXI) as a model. The structures were rebuilt in COOT [29], with cycles of refinement in REFMAC5 [30]. Holobacterioferritin (BFR with cofactors bound) forms a spherical shell, but the apo-bacterioferritin with no heme group forms crystallographic dimers in the crystal lattice, with one monomer in the asymmetric unit. Detailed parameters and diffraction data are available within the supplementary information (Supplementary Table 1). Structure coordinates and structure factors have been deposited in the PDB (4CVP, 4CVR, 4CVS and 4CVT).

2.5. Isothermal calorimetry (ITC)

A VP-ITC Calorimeter (MicroCal™) was used to study manganese binding to apo-BFR protein variants. The samples were degassed using a rotary vane vacuum pump at 23 °C before loading into the instrument. Titrations were performed as 11 μl aliquots of 900 μM $MnCl_2$ into a 30 μM solution of BFR[1] [6]. The raw data generated from ITC was fitted to either a least squares model or a two-site model with the Microcal ™ VPViewer 2000 ITC data analysis fitting software (Version 1.30) on Origin 7.0.

2.6. EPR measurements

EPR experiments were undertaken using a Bruker Elexys E500 Spectrometer (Bruker BioSpin, GmbH) with a super X-band microwave bridge running in perpendicular mode at 9.44 GHz. Low temperature measurements were performed using a helium cooled Oxford ES-900 cryostat and an Oxford ITC-4 temperature controller. All spectra were recorded using the Bruker X-EPR software system. Data subtractions, manipulations and analysis were done using either the Bruker X-EPR software or Bruker WinEPR. The samples were prepared in the dark or under very low green light at room temperature to a final concentration of 300 μM with TBS + 20% glycerol (cryoprotectant). The metal (Mn) or pigment ($ZnCe_6$) co-factors under study were added in stoichiometric amounts. The samples were degassed using a rotary vane vacuum pump and maintained under anaerobic conditions with either gaseous argon or nitrogen. All samples were frozen initially in a dry-ice/EtOH bath followed by liquid nitrogen, before loading into the cavity. All spectra were taken within 48 h after sample preparation. Samples were

[1] The data was collected by the Water Resources Group-Analytical Services; ALS Environmental Facility, Canberra, Australia.

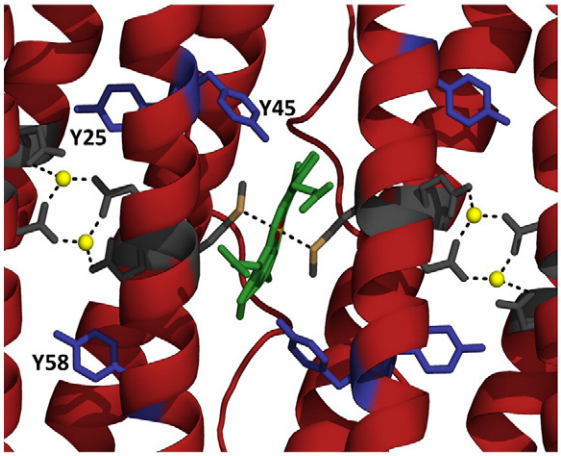

	$ZnCe_6$	Metal
Distance in Å from cofactor		
Y10	21	18
Y25	14.5	4.3
Y45	3.1	15.8
Y58	12.6	6.4
Y107	23.9	22.4
Y114	28	24.7
Y149	21.4	16.4

Fig. 3. Three tyrosine residues; Y25, Y58 and Y45 (blue sticks), bound metal $Mn^{II, II}$ (yellow spheres), metal ligand residues (grey sticks), heme binding site with methionine residues as ligands (grey sticks colour coded by atom type) in *E. coli* BFR. These were mutated to phenylalanine to remove the redox active –OH group. Table to show respective distances of the - OH group of the seven Tyr residues per *E. coli* BFR monomer from the photoactive pigment $ZnCe_6$ and the nearest metal ion. The three Tyr residues within the electron tunnelling distance are highlighted (black box).

illuminated using continuous white light (200 W Sony slide projector lamp) for 5 s, for light-dependent EPR measurements, unless otherwise stated.

2.7. Cyclic voltammetry

Cyclic voltammetry was performed using a PAR 263A potentiostat equipped with a conventional three electrode cell containing, glassy carbon working electrode (3 mm diameter), Ag/AgCl reference electrode (saturated KCl) and platinum wire counter electrode; scan rate was 100 mV/s. The potential quoted here are against normal hydrogen electrode (NHE). $ZnCe_6$ redox potential measurements were performed in glycine buffer saline (25 mM glycine, pH 10, 25 mM NaCl) and 100 mM KCl was added as supporting electrolyte. The sample was kept under N_2 purge at all times. Light driven oxidation was minimised by conducting the measurement under safe green light.

3. Results

3.1. Structure of bacterioferritin tyrosine variants

It was first necessary to structurally characterise each of the three bacterioferritin homodimer tyrosine variants which were investigated here. This was done by using X-ray crystallography to probe for any structural changes induced by mutagenesis. All structures were resolved to 2.1 Å or better. The maximum pairwise Cα RMSD between the structures is 0.5 Å, and the minimum is 0.1 Å. The di-metal site differed between these depending on the preparation and crystallisation conditions. The BFR^1 form had iron (see PDB), Y45F cadmium, and the Y25F and Y58F had Zn. Fig. 4a shows the crystal structures of the monomeric subunit (four-helix bundle) of each of the BFR tyrosine variants, overlayed. A comprehensive 3-D analysis of these protein variants indicated that these changes are conservative and quite subtle for BFR variants Y25F (red) and Y58F (green). However, for BFR variant Y45F (blue) the structural changes are slightly more pronounced (Fig. 4a). The crystal structure shows that mutating tyrosine 45 to phenylalanine slightly perturbs the orientation of the phenyl ring facing towards the hydrophobic pocket at the dimer interface, and has an allosteric effect on the position of Y25 (Fig. 4a). All variants reveal correct folding into an alpha helix bundle and also show binding of the metal (Fe, Zn or Cd) at the di-nuclear metal site. A super-position of the metal binding sites of each BFR tyrosine variants is shown in Fig. 4b. This confirms that at the 3-D structure level, upon Y25F or Y58F mutation, the ligand environment of the metal binding remains essentially unaltered with the same patterns of binding; whereas the Y45F mutation (blue) slightly affects the position of the Y25 side chain which is rotated so that the terminal O atoms moves by 2.3 Å but is still hydrogen bonded to E94, a direct ligand to the metal [15].

Table 1
Absorbance maxima at Soret and Qy wavelengths (nm) for BFR-homodimer variants bound to $ZnCe_6$.

	Peak-position (nm)	
Protein	Soret	Q_y
$ZnCe_6$-no protein	412	633
BFR^1	419	638
Y25F	421	637
Y58F	414	637
Y45F	413	637

3.2. Cofactor assembly

3.2.1. $ZnCe_6$ binding to BFR^1 and tyrosine variants

Binding of $ZnCe_6$ to the BFR variants was monitored using UV–visible spectroscopy. Adventitious binding of the pigment to the protein was inhibited by using the BFR^1 variant (methods). The optical spectra of $ZnCe_6$ bound to BFR are shown in Fig. 5, as shifts in the Soret, Q_x and Q_y bands relative to $ZnCe_6$ in aqueous solution. All BFR variants produced comparable optical spectra. $ZnCe_6$ bound to each BFR^1-homodimer variant showed about 5 nm red-shit in the Q_y region (633 nm → 638 nm) and a similar (5–8 nm) red-shift in the Soret absorbance (412 nm → 421 nm) (Table 1).

3.2.2. Manganese binding to BFR^1 and tyrosine variant (ITC and EPR measurements)

The data from ITC measurements of Mn^{II} binding to each of the apo-BFR variants, observed by titration of fixed aliquots of Mn^{II} into a solution of the peptide, are presented in Fig. 6. In each case, the figure shows the time resolved injection heat for metal ion binding to the protein (top panel) and the integrated heat of reaction for each injection (bottom panel). The raw data obtained for each variant were fitted using the best fit of a standard least squares model for two-independent binding sites to obtain a binding profile for each variant. The fitting was performed over several statistical iterations, and the derived thermodynamic and binding constants, presented here are considered reliable within ~25% reported values. All engineered apo-BFR variants showed binding of at least two metal ions per protein

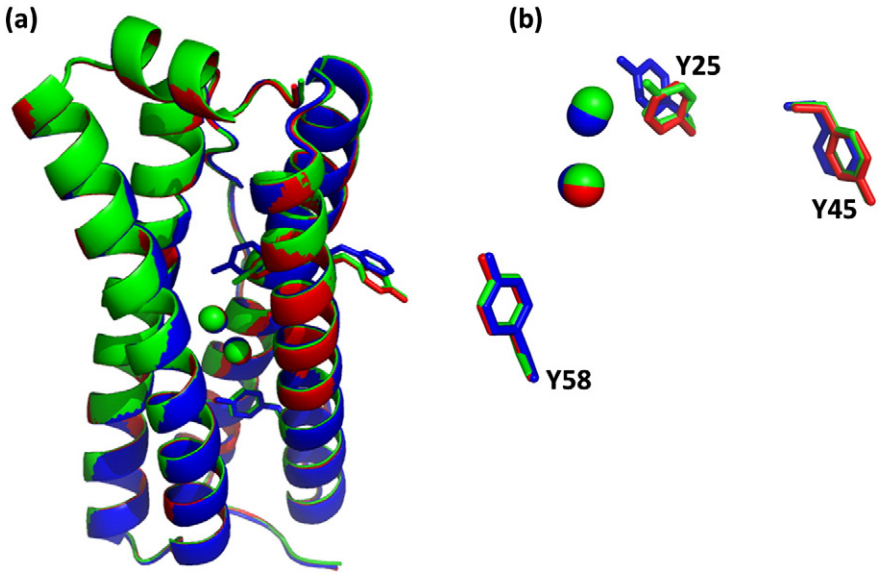

Fig. 4. Super-position of the crystal structures of the three BFR tyrosine variants at 2.1 Å resolution. (a) Y25F (red), Y58F (green) and Y45F (blue) presented as a super-position of the monomeric subunit. The bound metal (sphere) is also shown; Y25F (cadmium) and Y58F and Y45F (zinc); (b) model of the super-imposed metal binding site for each variant.

monomer with varying binding affinities. Titration data of Mn^{II} binding to these variants also indicated that each binding site has a distinct thermodynamic component associated with metal ion ligation to that site (Table 2).

In BFR[1], the first metal binding is an exothermic process with a higher binding affinity ($K_{a1} \sim 0.7 \times 10^7\ M^{-1}$) compared to the second ion binding which is a weakly endothermic process with a lower binding affinity ($K_{a2} \sim 2 \times 10^5\ M^{-1}$). The binding stoichiometry derived was an average of 2.2 moles of Mn^{II} ions per mole of BFR[1]. The tyrosine variant Y25F showed Mn^{II} binding averaging at 2.7 moles of Mn^{II} per mole of protein, where the second ion binding indicated to be weakly exothermic (Fig. 6 and Table 2).

Ligation of Mn^{II} ions to the Y58F variant was thermodynamically distinct from the other BFR variants (Fig. 6). Whilst the calorimetric data was fit to a two binding site model, it was found to also fit well to the sequential binding model of three sites with different binding constants (*data shown here is based on the two-site binding model*). The binding constants derived from data-fitting show two distinct binding constants ($\sim 10^7\ M^{-1}$ and $\sim 10^5\ M^{-1}$), however with significantly large uncertainties (~90%), making it difficult to interpret the precise affinities of the two sites relative to other BFR variants, even though they are within the same orders of magnitude. Nevertheless, the binding stoichiometry obtained was an average of 2.9 moles of Mn^{II} per mole of Y58F. It is apparent from Fig. 6 (and from the three site fitting) that most of the 'two Mn loading' appears to occur with no obvious separation of the individual steps and is net endothermic in nature. This might indicate quasi-concerted or effectively 'independent' binding (see discussion Section 4.2). The third site binding is the weakest, also with endothermic character and the crystal structures do not reveal it for the Fe^{II} bound protein case (Fig. 4). It may be superficially located. In the case of Y45F, the ITC data shows that the variant also binds an average of 2.9 moles of Mn^{II} per mole of protein. Within a two site model, this variant was also found to have different binding constants for the two sites ($K_{a1} \sim 0.09 \times 10^7\ M^{-1}$ and $K_{a2} \sim 0.08 \times 10^5\ M^{-1}$), but relatively weak (Table 2).

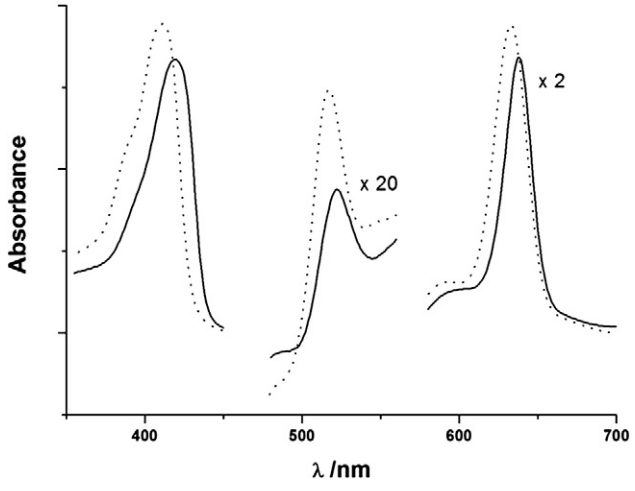

Fig. 5. Spectroscopic determination of $ZnCe_6$ binding to the modified BFR. UV–visible spectra of $ZnCe_6$ free in solution (dotted line) and ligated with BFR[1] (solid line). Experimental: all samples were in TBS buffer (pH 7.5).

EPR spectroscopy was used to investigate the paramagnetic properties of Mn^{II} bound at the di-nuclear site of the engineered BFR scaffold ($\pm ZnCe_6$) and the associated coupling environment. The EPR spectra were recorded at three temperatures (15 K, 25 K and 55 K) for each BFR variant to which stoichiometric amounts of Mn^{II} per mol of BFR were added. The spectrum of bound coupled Mn^{II} for each of the BFR variants was obtained by performing scaled subtractions of the unbound and bound uncoupled monomeric Mn^{II} 'six-line' spectrum. Estimates of the stoichiometry for the protein bound Mn^{II} were also made by this scaled subtraction for each BFR variant (Table 3). The overall spectra of Mn^{II} ligated to the protein revealed a broad line shape (peak to peak width ~680–700 G) centred at ~$g = 2$ for each variant (Fig. 7). These are very similar to those seen by Khangulov *et al.* [31] and arise principally from the $S = 1$ state of a weakly antiferromagnetically coupled Mn^{II}–Mn^{II} dimer, where the ground state has spin 0, and the excited states are $S = 1, 2\ldots$[31,32]. The curie temperature dependence of the spectra for all variants (Supplementary Fig. A.1), analysed as in [31], suggests that the exchange coupling, J, magnitudes for the BFR and Y58F variants are ~5–6 cm^{-1}, whilst those for the Y25F and Y45F variants are ~3–4 cm^{-1}. These are typical of known Mn^{II}–Mn^{II} dimer systems [31], with Mn–Mn separations in the range ~3.3–3.8 Å. The crystal structures obtained here contained Zn or Cd in the di-nuclear metal sites (no $ZnCe_6$ bound at dimer interface), but the range of metal–metal separations seen, 3.6–4.1 Å are generally consistent with the EPR data. We did not attempt to analyse

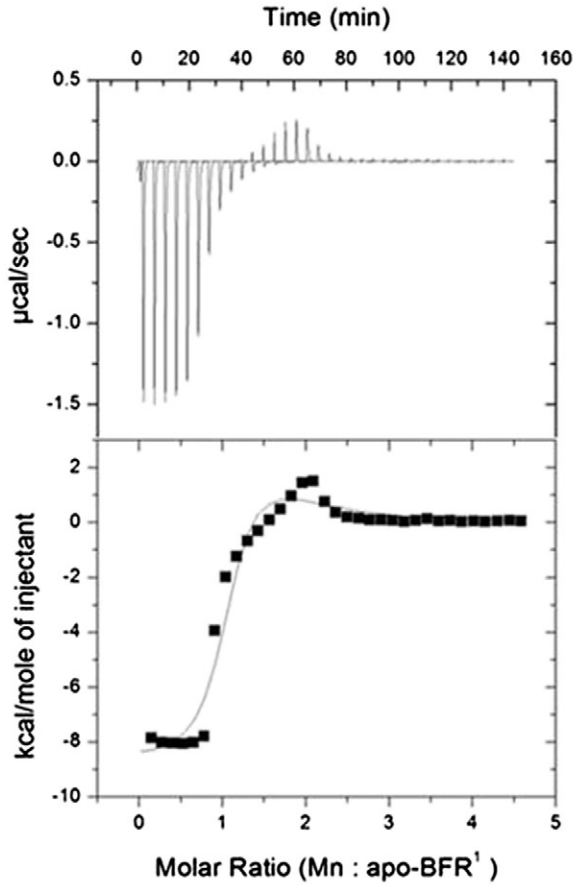
Time (min)
µcal/sec
kcal/mole of injectant
Molar Ratio (Mn : apo-BFR[1])

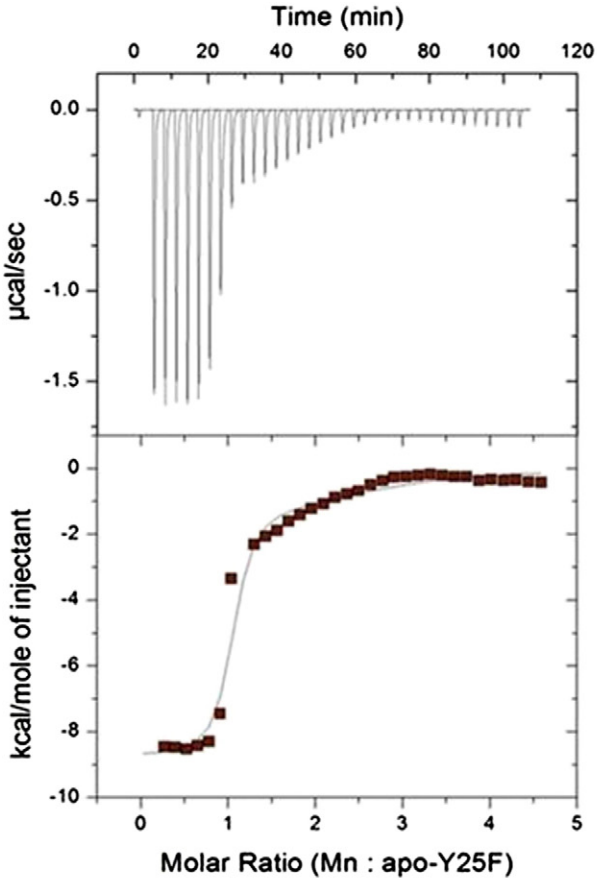
Time (min)
µcal/sec
kcal/mole of injectant
Molar Ratio (Mn : apo-Y25F)

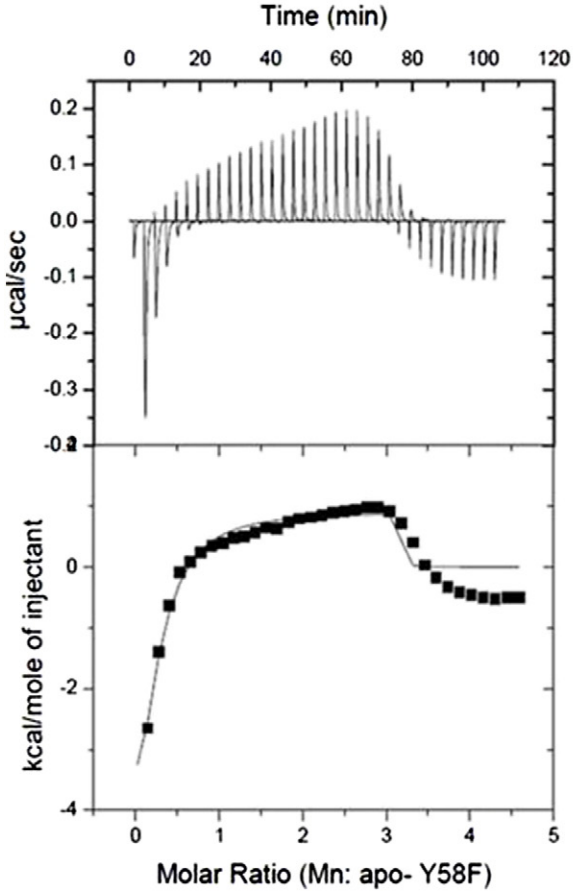
Time (min)
µcal/sec
kcal/mole of injectant
Molar Ratio (Mn: apo- Y58F)

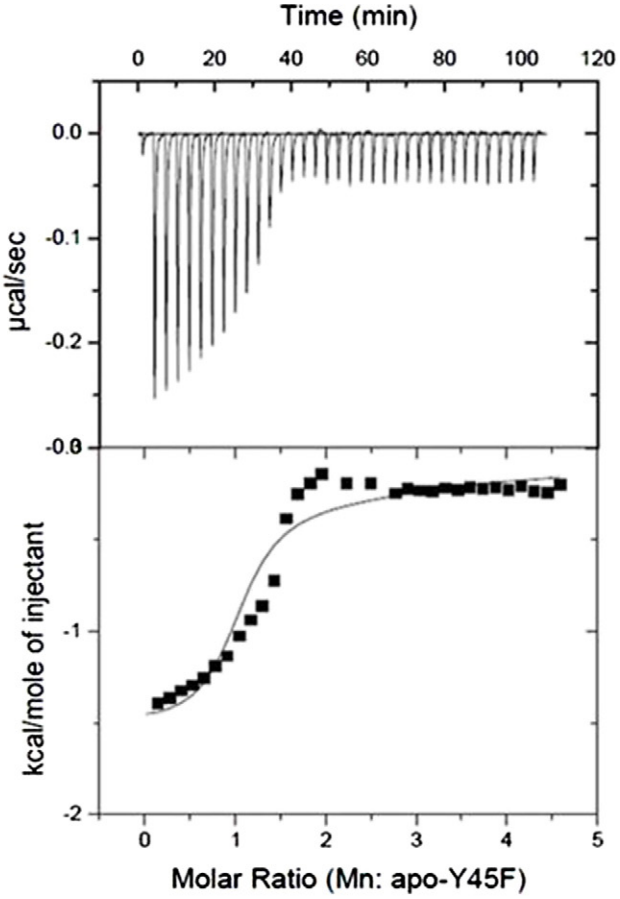
Time (min)
µcal/sec
kcal/mole of injectant
Molar Ratio (Mn: apo-Y45F)

Table 2
Thermodynamic and binding constants for calorimetric titration of Mn^{II} into the modified apo-BFR. Parameters derived by best-fit of the data points to a two-independent binding site model. n.d.*—binding constants for Y58F not determined due to statistically significant errors.

	Mn^{II} titrated into apo-BFR mutants							
	n_1	K_{al} ($\times 10^7$ M^{-1})	ΔH_1 (kcal mol^{-1})	ΔS_1 (cal mol^{-1} K^{-1})	n_2	K_{a2} ($\times 10^5$ M^{-1})	ΔH_2 (kcal mol^{-1})	ΔS_2 (cal mol^{-1} K^{-1})
BFR[1]	1.05	0.66	−8576	2.45	1.20	1.99	2530	32.7
Y25F	1.00	1.53	−8758	3.50	1.70	1.05	−1527	17.8
Y58F	0.2	n.d.*	−8175	9.97	2.75	n.d.*	973	35.7
Y45F	1.00	0.09	−1510	13.6	1.95	0.08	−1248	22.1

Table 3
Table to show percentage (%) Mn^{II} bound (coupled) to each BFR variant relative to uncoupled Mn^{II} in buffered solution.

BFR mutant	(%) Mn^{II} bound and magnetically coupled
BFR[1]	55
Y25F	50
Y58F	25
Y45F	20

further or simulate the spectral shapes in Fig. 7, as these typically also contain contributions from quintet ($S = 2$) or even higher states and require definition of the relevant fine structure terms [31]. The latter require identification of the quintet resonances in the $g \sim 4$ region, at least, for reliable estimation and that was not performed here. However, the ~40 G low field and up field hyperfine spacing (i.e. half the ~90 G hyperfine spacing of isolated Mn^{II}) is consistent with our identification of the $g \sim 2$ region resonances coming principally from the $S = 1$ state of a $Mn_2^{II,II}$ dimer.

The addition of the $ZnCe_6$ pigment to the protein with bound manganese (BFR[1] + Mn) revealed spectra that had similar overall spectral features to samples measured in the absence of bound $ZnCe_6$ for all variants investigated (Fig. 8). The spectrum shown here is of Y25F, where the width of the total spectrum is between 580 and 630 G for each temperature (15 K, 25 K and 55 K), centred at ~$g = 2$ (other BFR variants displayed similar spectral features, not shown). Although, the experimental conditions were optimised to prevent light-exposure to the samples, a photo-oxidised $ZnCe_6$ species was observed due to a small amount of inadvertent light exposure during sample preparation. Integration of this narrow radical signal indicated that in dark typically <15% of $ZnCe_6$ radical is formed. The temperature dependence of the broad Mn signal is nominally Curie and appears to indicate that the (weak) Mn–Mn coupling changes from anti-ferromagnetic to near zero (probably still anti-ferromagnetic, Supplementary Fig. A.2) in the presence of $ZnCe_6$ bound to the protein. This presumably is due to slight structural changes within the protein, altering the bridging between the two Mn ions. This is known to be somewhat variable in ferritins [33], with an oxy species, likely a water molecule, variable present between the metal ions.

3.3. Light-induced electron transfer—EPR spectroscopy

3.3.1. BFR[1]–$ZnCe_6$ and tyrosine oxidation

Light induced oxidation of protein bound $ZnCe_6$ was readily observed by EPR spectroscopy under non-saturating microwave power and optimum temperature of sample illumination, 0.8 μW and 250 K respectively. The oxidised $ZnCe_6^{\bullet+}$ EPR spectrum observed upon illumination of the BFR[1]–Z complex (±Mn bound) is centred at $g = 2.0023$ and has a peak-to-peak (p–p) width of ~6.8 G (Fig. 9a). Double integration of the signal revealed that 100 (±15)% of $ZnCe_6$ added to the BFR sample is oxidised upon illumination, measured by spin count using a Cu^{2+} ($CuSO_4$) standard at the same molar concentration, with the same EPR parameters.

With the Mn^{II} dimer bound at the di-nuclear binding site of BFR (~55% centres), i.e., in the BFR[1]-Z (+Mn) complex, a mixed paramagnetic signal was observed (Fig. 9b). This combined spectrum was resolved to be a narrow $ZnCe_6^{\bullet+}$ radical and a broader ~24 G spectrum, centred at $g = 2.0048$ (Fig. 10). The wider spectrum was assigned to oxidised tyrosine radical ($Y^{\bullet}$) species owing to (i) spectral similarities (line-width and g-value) to oxidised tyrosine species observed in other natural and modified proteins [13,14] and (ii) the proximity of tyrosine residues to the photoactive pigment in the BFR protein able to act as effective electron donors to the oxidised $ZnCe_6^{\bullet+}$. The possibility of a contribution from a reduced quinone electron acceptor species was eliminated as the samples were prepared in the absence of a quinone molecule. There were no other identified active paramagnetic centres in this system that could be readily assigned to radicals (particularly with this shape) in the EPR spectrum. In the BFR protein sequence there are only two tryptophan residues and there are no cysteine (sulphur centres) residues. The possibility of a paramagnetic tryptophan derived species cannot be completely eliminated without further investigation. However, it is noted that tryptophans oxidise at potentials 100–150 V above tyrosine and would be expected to be less favoured than tyrosine to undergo oxidation [34].

A spin count comparison by evaluating the double integral of the $ZnCe_6^{\bullet+}$ radical (±Mn) and the $Y^{\bullet}$ radical (the latter formed only in the presence of Mn), suggested that the reaction centres that contain the $ZnCe_6^{\bullet+}$ radical in the absence of Mn, are replaced by almost 90% oxidised $Y^{\bullet}$ in the presence of bound $Mn_2^{II,II}$, with all other variables kept constant (Table 4). To further investigate the effects of the bound Mn^{II} as an active paramagnetic centre in the engineered BFR reaction centre, power saturation behaviour of both the $ZnCe_6^{\bullet+}$ and $Y^{\bullet}$ species generated from the BFR[1]-Z (+Mn) complex post-illumination was explored. This study showed that the $P^{1/2}$ for the $ZnCe_6^{\bullet+}$ radical increased to 15.4 (±2.2) μW compared to 1.839 (±0.1) μW in the absence of bound Mn^{II} dimer. Saturating powers for the $Y^{\bullet}$ radical were not reached up to 32 μW (Supplementary Fig. B).

3.3.2. BFR[1]/tyrosine variants—$ZnCe_6$ and tyrosine oxidation

The site-specific variants (Y25F, Y58F and Y45F) of the BFR[1] protein-scaffold were designed to elucidate the photochemical pathways of tyrosine oxidation in this engineered 'reaction centre'. Upon illumination, the $ZnCe_6$ bound at the fully assembled BFR dimer interface, was photo-oxidised forming a cation radical species $ZnCe_6^{\bullet+}$ (p–p ~ 6.8 G and ~$g = 2.0023$) in all three tyrosine variants. However, an EPR spectrum 20–24 G wide was also resolved in each of the variant after subtracting the $ZnCe_6^{\bullet+}$ radical. The measured g centre values (with a g-uncertainty of ±0.0002) for these are given in Table 5. The spectral features, notably line width and the g-value, as well as the apparent effect of tyrosine mutations on the total spin-count of the observed spectrum, was used to assign these to oxidised tyrosine species in all BFR-tyrosine variants (Fig. 11 and Table 5). Like BFR[1], the tyrosine

Fig. 6. Calorimetric titration of $MnCl_2$ into a solution of apo-BFR[1] (and variants). For each BFR variant; raw ITC output (top panel), integrated raw data (bottom panel, scattered points) and best-fit to a least squares model for two independent sites (bottom panel, solid line) are shown. Experimental: 7 μl injections of 900 μM $MnCl_2$ were titrated into a 30 μM solution of protein. Both the titrant and the macromolecule were prepared in TBS buffer, pH 7.5. A heat of dilution blank ($MnCl_2$ titrated into TBS buffer) has been subtracted from each plot shown.

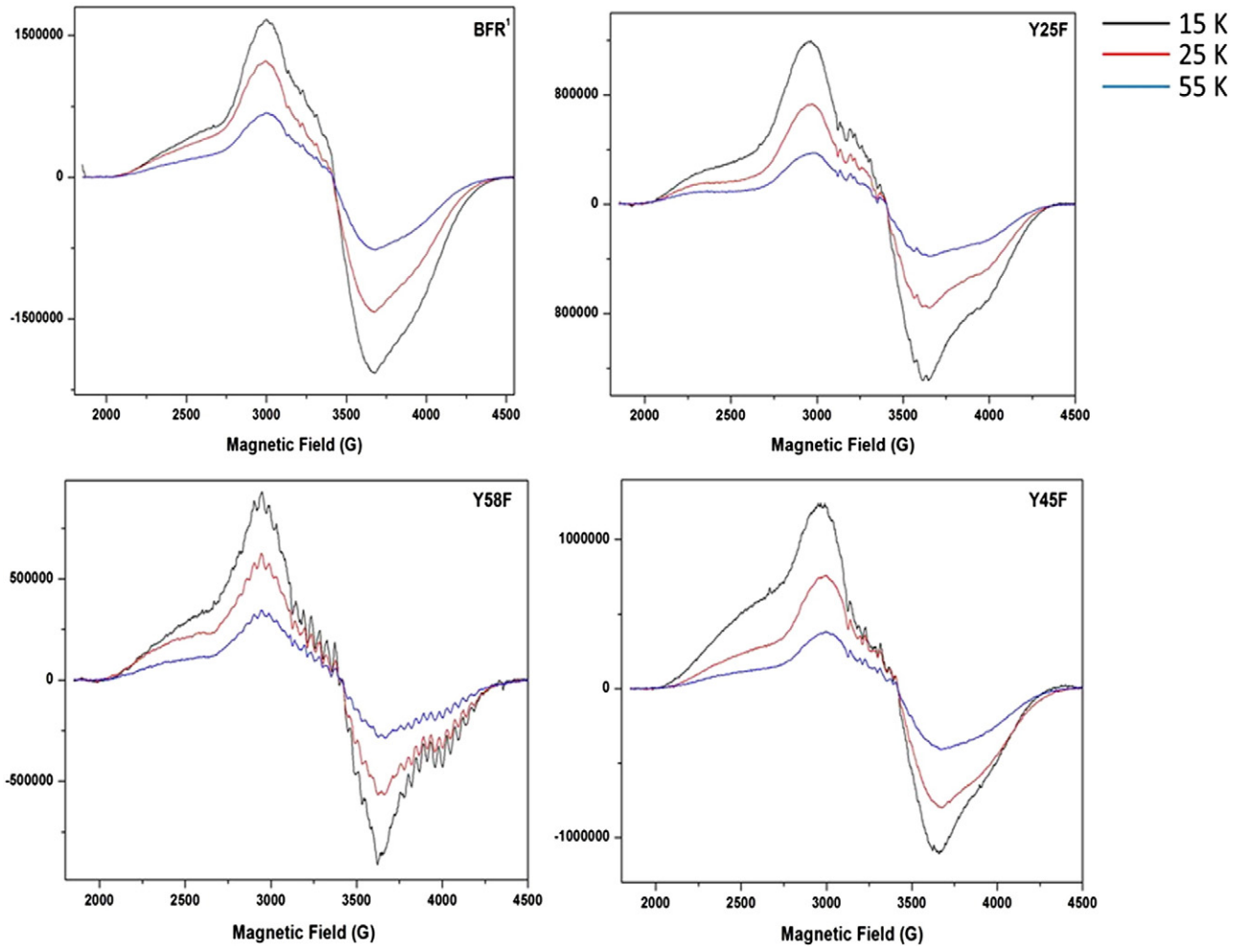

Fig. 7. EPR spectra of $Mn_2^{II,II}$ bound to BFR variants (−$ZnCe_6$). All spectra are drawn as magnetic field (abscissa) versus signal amplitude (ordinate) for three temperatures; 15 K (black), 25 K (red) and 55 K (blue). Experimental: microwave frequency 9.44 GHz, microwave power 500 μW, and modulation amplitude 10 G. See Supplementary Fig. C for EPR Spectra of Mn^{II} in buffered solution (i.e., unbound to the protein).

variants were illuminated in the absence of a quinone electron acceptor, which removes the possibility of the reduced quinone contribution to the observed spectrum. A quantitative analysis of the photo-oxidised porphyrin and the ~20–24 G wide species in all BFR/tyrosine variants-

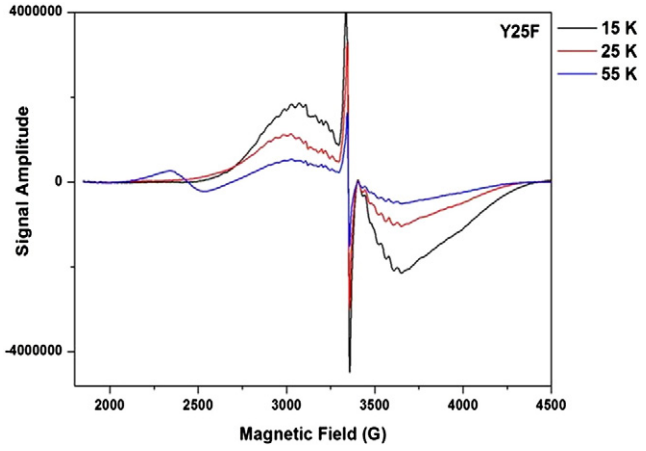

Fig. 8. Temperature dependence of $Mn_2^{II,II}$ bound to BFR (+$ZnCe_6$). EPR spectrum of BFR/Y25F with bound cofactors (+Mn, +$ZnCe_6$) at three temperatures; 15 K (black), 25 K (red) and 55 K (blue) plotted as magnetic field (abscissa) and signal amplitude (ordinate). *Similar EPR spectra were seen for other BFR variants.* Experimental: minimal light, microwave frequency 9.44 GHz, microwave power 500 μW, and modulation amplitude 10 G.

Z (+Mn) showed that the spin populations of the two differ remarkably between variants (Table 6).

The integrated intensity of the presumed $Y^{\bullet}$ species is reduced to about ~54% in the Y45F compared to ~85% for both Y25F and Y58F variants on a per BFR dimer basis (Table 6).

Finally, preliminary simulations of these $Y^{\bullet}$ radical spectra using EasySpin Hamiltonian formalism indicated that although there are spectral similarities to tyrosine radicals, this signal cannot be assigned to a single oxidised tyrosine species using conventional tyrosine hyperfine couplings for the ring protons and methylene group.

Redox potential of $ZnCe_6$ in solution, pH 10 (not bound to the BFR-RC in the absence of Mn), was also measured directly. Cyclic voltammetry of a solution of $ZnCe_6$ reveals an oxidation wave with peak potential at 0.583 V (vs. NHE) and a corresponding reduction wave at 0.496 V (Supplementary Fig. D). The observed oxidation/reduction couple is quasi-reversible with $E_{1/2} = 0.540$ V. At higher potentials, the voltammogram become ill defined with presence of multiple oxidation waves.

4. Discussion

4.1. Crystal structures

High-resolution crystal structures of BFR variants Y25F, Y58F and Y45F were successfully obtained in the presence of metals bound to the di-nuclear metal binding site. The overall 3-D structure observed for all variants is conserved (Fig. 4) and compares well with other

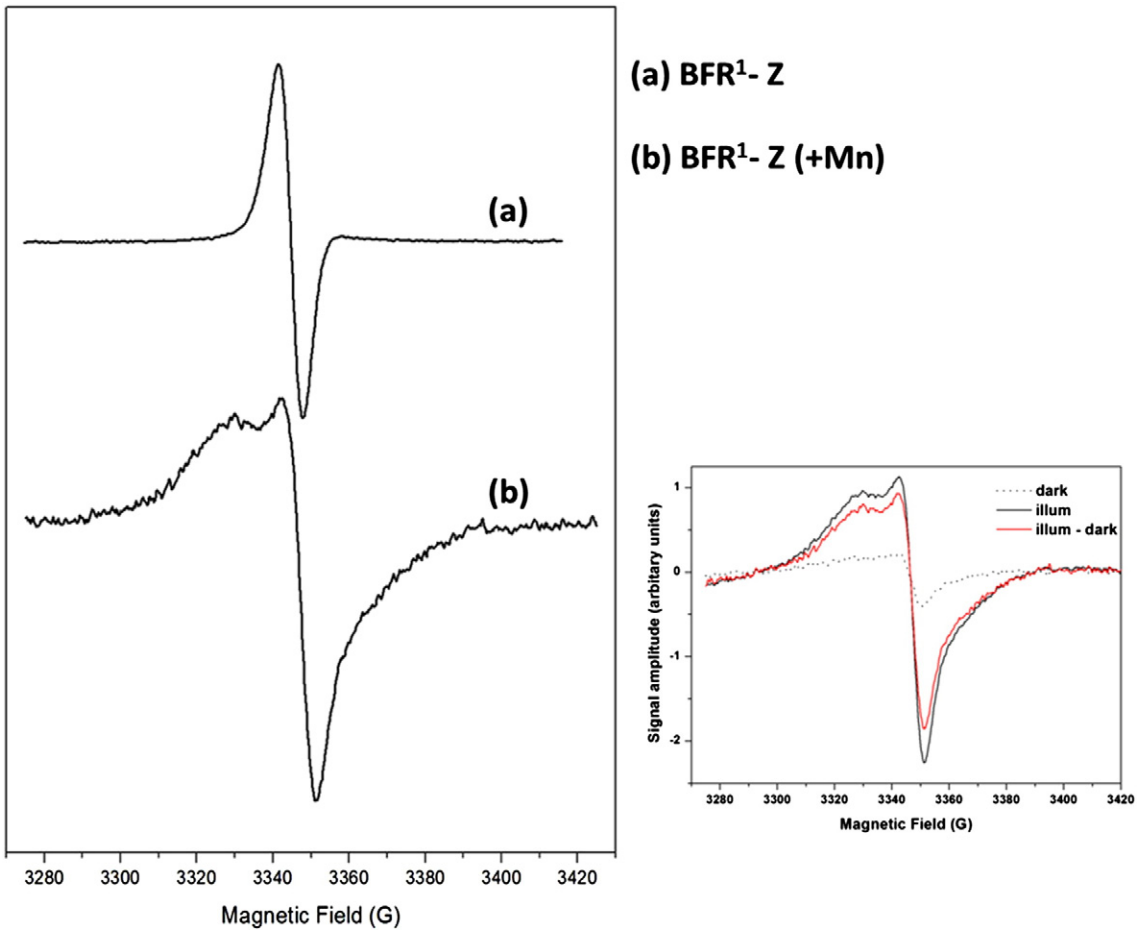

Fig. 9. EPR spectra of the light-induced BFR[1]- Z (±Mn) complex. (a) Spectra show a narrow $ZnCe_6^{\bullet+}$ radical with p–p width ~6.8 G, centred at $g = 2.0023$ and (b) Spectra show the $ZnCe_6^{\bullet+}$ radical combined with a $Y^{\bullet}$ radical; which has been resolved in Fig. 10. Experimental: microwave frequency 9.44 GHz, microwave power 0.8 μW, modulation amplitude 2 G, and cavity temperature 25 K. Both samples were continuously illuminated (5 s) with white light at 250 K and 295 K for samples (a) and (b) respectively. Relevant dark spectrum has been subtracted from each, example shown in the inset, where dark spectrum (dotted) is subtracted from the illuminated sample (black) to generate the net spectrum (red).

resolved *E. coli* BFR crystal structures [9,10]. The monomeric subunit shows folding into a four α-helix bundle capped by a short fifth helix at the C-terminal end (Fig. 4a).

Detailed amino acid sequence alignment analysis of *E. coli* BFR and other ferritins shows that Tyr25 is a conserved residue at that position [10,15]. The residue is near the di-metal site and a crystal structure comparison of *E. coli* BFR with the BFR from *Azotobacter vinelandii* in the absence of a bound metal, indicates about 70° rotation differences of Tyr25 between the two cases [35]. Tyr58 is unique to *E. coli* BFR and is replaced by Ile or Leu in other BFRs [10]. Tyr45, which is within van der Waals contact of the hydrophobic pocket for haem binding in *E. coli* BFR, is not conserved at this position amongst other ferritins and is commonly replaced by either a Glu or an Arg residue [10].

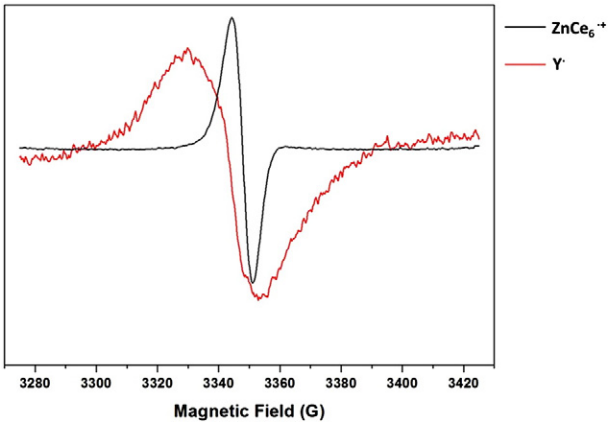

Fig. 10. EPR spectra for the BFR[1]- Z (+Mn) complex resolved to show the oxidised $ZnCe_6$ (black) and the oxidised tyrosine species (red). The resolved $Y^{\bullet}$ is ~24 G wide and is centred at $g = 2.0048$.

In the crystal structures provided here, it is clear that substituting Y25 and Y58 with a phenylalanine residue has negligible effect on the overall 3-D structure of the protein and the metal binding site. However, substituting Y45 with a phenylalanine slightly perturbs that residues' orientation towards the haem pocket, as well as induces an allosteric effect on the orientation of the Y25 phenol ring (Fig. 4). These small conformational changes can be attributed to minor changes in the protein hydrogen bonding network.

Although Tyr25 has an altered position in the Y45F variant, its hydroxyl group (–OH), remains virtually the same distance (4.4 Å) from the nearest metal. The distance of the –OH group of Y25 from the porphyrin binding site also remains unchanged in the Y45F form. It is then reasonable to assume that the light-induced electron transfer

Table 4
Comparing contributions of $ZnCe6^{\bullet+}$ and $Y^{\bullet}$ oxidised species in illuminated BFR[1]-Z (±Mn). DI: double integral (machine units) for each signal as measured using WINEPR.

	$ZnCe_6^{\bullet+}$ (DI)	$Y^{\bullet}$ (DI)	Approx. % $ZnCe_6^{\bullet+}$	Approx. % $Y^{\bullet}$
BFR[1]-Z (-Mu)	$235e^9$	n.d.	100	0
BFR[1]-Z (+Mn)	$2.90e^8$	$2.31e^9$	11	89

Table 5
Table comparing spectral features of the total tyrosine radical observed in the three tyrosine variants. The *g*-values for these spectra can be estimated to be better than ~0.5 G in 3500 G. *g*-uncertainty to be ±0.0002.

BFR-tyrosine mutant ($Y^{\bullet}$)	*g*-factor	p–p distance (G)
Y25F	2.0042	24.2
Y58F	2.0044	24.5
Y45F	2.0038	20

Table 6
Table comparing contribution of $ZnCe_6^{\bullet+}$ and $Y^{\bullet}$ oxidised species in illuminated BFR-Z (+Mn) for the three tyrosine variants. DI: double integral for each signal as measured on WINEPR (machine units). The integrals are accurate to ~1%, i.e., ±1% from baseline estimation.

Tyrosine mutant	$ZnCe_6^{\bullet+}$ (DI)	$Y^{\bullet}$ (DI)	Approx. % $ZnCe_6^{\bullet+}$	Approx. % $Y^{\bullet}$
Y25F	$8.099e^8$	$4.336e^9$	16	84
Y58F	$3.562e^8$	$2.061e^9$	15	85
Y45F	$1.580e^9$	$1.885e^9$	46	54

analysis of Y45F is independent of the 'small' alterations in the electron-tunnelling distance between the redox active tyrosine residue and bound cofactors.

4.2. Cofactor assembly

In BFR, the haem binds with a non-covalent axial ligation to the methionine residues through the Fe^{II} centre. In this work, the haem was replaced by $ZnCe_6$ and its binding to the protein was monitored by spectral shifts in the pigment absorption bands (Soret band, 412 → 419 nm and Q_y band, 633 → 638 nm) for all BFR variants. This red-shift in the $ZnCe_6$ spectra upon protein binding is consistent with previous work on BFR and also for $ZnCe_6$ binding to other peptides [19,24]. These shifts are attributed to the change in the ligand environment of $ZnCe_6$ (aquo to thiol ether). It is known that the Q bands of the porphyrins are more sensitive to the changes in the microenvironment and the protonation state of the pyrrole ring than the Soret bands [36].

Reconstitution of the apo-BFR protein scaffold with Mn^{II} at the di-nuclear metal binding site was investigated using ITC and EPR spectroscopy. It is known that, the absence of haem does not significantly affect the stoichiometry of binding of class II metals to the *E. coli* BFR [37,38]. The ITC measurements were conducted on apo-BFR (-$ZnCe_6$), whilst EPR spectroscopy was used to investigate BFR (±$ZnCe_6$) forms.

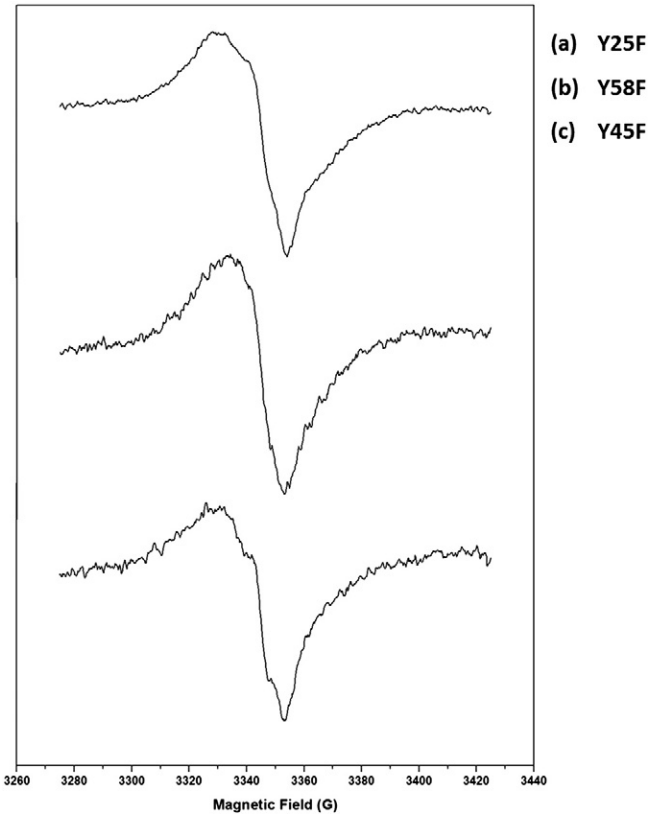

Fig. 11. EPR spectra of the resolved tyrosine radical signals in three BFR tyrosine variants, upon illumination. (a) Y25F, (b) Y58F and (c) Y45F. The *g*-values and p–p distance for each is given in Table 5.

Thermal calorimetry data for Mn^{II} binding to the BFR^1 form has previously been reported in [6]. However, the ITC data for Mn^{II} ligation at the metal binding sites of BFR tyrosine variants (Y25F, Y58F and Y45F) is presented here for the first time. The stoichiometry of Mn^{II} binding to BFR^1 derived from the ITC data was an average of 2.25 mol of Mn^{II} ions/mol of protein. This compares well with the previously reported average of 2.5 (±0.12) mole of Mn^{II} to one mole of BFR^1 [6]. It is known that there are low-affinity, non-specific binding sites for metal ions on the BFR surface which can account for the small amount of metal binding above the stoichiometry of 2:1 (metal:BFR). It is also known that metal binding to these low-affinity sites is secondary to binding at the di-nuclear binding site [39].

Note that, previous structural studies of wild-type BFR from various species indicate that the two metal sites in the protein do not bind Fe^{II} homogenously; generally only one metal site shows full occupancy [35]. This is consistent with the present findings of calorimetric titrations of Mn^{II} for the two sites, where one site typically shows substantially stronger metal affinity than the other for all three BFR variants.

When compared to the previously reported binding constant for the BFR^1–Mn^{II} interaction using ITC [6], the binding constants reported here are only somewhat different. These differences can be attributed to the variations in buffer conditions and ITC parameters used for the experiments, as well as the fitting of the curves, which can affect precise values of the numerical data generated by this technique [40]. In the case of BFR, we know that the binding of cofactors induces formation of multimers of the protein, which can also contribute significantly to the heat changes observed in the ITC measurements, depending on the experimental conditions used.

The observed heat changes upon metal–BFR interaction arise from changes in the ligand nature/network of each metal ion binding [39]. The formal ligand environments of the two assembled metals in the BFR protein variants are very similar, with carboxylate-histidine ligation from the peptide (and possibly bridging oxy species [33]). The high affinity and exothermic heat change seen for the first metal binding – contrasting with the much lower apparent affinity and weak exo/endo – thermic change of the second, reflects anti-co-operative binding. This is presumably electrostatic in origin, since both ions have +2 formal charge. For the Y58F variant, although a minority of centre (~20%) behave like the above, most metal loading occurs in what is likely a co-operative manner, with weak net endothermic change. Y58 is close enough to this di-metal site that loss of H-bonding interaction following mutation may be responsible for this effect (Fig. 3).

The average disassociation constant (K_d) for metal binding is; $K_d = 1/K_a$. The BFR variants displayed different binding affinities for Mn^{II} for the two sites, with general order, $BFR^1 \geq$ Y25F > Y45F. The association constant for Y58F could not be derived due to statistically significant errors associated with the best-fit parameters. In *E. coli* BFR Y25 is hydrogen bonded to E94; a direct ligand to one of the metal ions [10]. However the Y25 mutation appears to be much less perturbing in this regard than the Y58F mutation, which is also close, but on the opposite side of the di-nuclear site (Fig. 4).

In the BFR^1 form, the first Mn^{II} binds at the di-nuclear site with an average K_d of ~1.5×10^{-7} M. It is known that in BFR, the binding affinity order is $Cu^{II} < Co^{II} < Zn^{II}$ with reported K_d values of ~2×10^{-5} M, 1×10^{-5}

M and 2×10^{-7} M respectively [38,39,41]. Since the K_d values for Zn^{II} and Mn^{II} binding at the site are similar, manganese was added to the apo-BFR^1 and tyrosine variants before the addition of $ZnCe_6$, to prevent any non-specific binding of Zn^{II} to the metal binding site.

In order to investigate Mn^{II} binding, oxidation states and the magnetic coupling interaction in the BFR^1 and BFR^1/Y variants (Y25F, Y58F and Y45F), EPR spectroscopy was used. EPR signals from the coupled di-nuclear Mn sites (Fig. 7) are very distinct from those of free (in frozen solvent), or uncoupled (e.g. singly bound in protein) Mn^{II} centres. The latter have a well-known 'six-line' hyperfine splitting, centred at $g \sim 2$ (Supplementary Fig. C) [42,43]. By subtracting scaled amounts of all free and bound uncoupled monomeric Mn^{II} 'six-line' contribution from the total Mn spectra, estimations of binding stoichiometry of di-nuclear manganese were made. This indicated that in BFR^1 and Y25F variant forms, 55% and 50% centres contain the paramagnetic $Mn_2^{II,II}$ pairs respectively. In Y58F and Y45F this is almost halved to 25% and 20% respectively under the given experimental conditions (Table 3).

The EPR spectral features and temperature dependence curves of the signals in the BFR-variants ($\pm ZnCe_6$) indicated that Mn^{II} binds at the di-nuclear binding site, as either an anti-ferromagnetically coupled (in $-ZnCe_6$) or as a near un-coupled pair ($+ZnCe_6$), in all variants (Figs. 7 and 8). A qualitative estimation of the coupling strength between the two bound metal-ions in ($-ZnCe_6$) indicated that in BFR^1 and Y58F, the exchange coupling is equally strong and is ~35–40% more than in Y25F and Y45F variants. Such coupling reveals that the two metal ions are bound at the site such that bond-mediated orbital overlap is permitted [42]. In the native *E. coli* BFR crystal structure with Mn^{II} bound at the di-nuclear centre, the two metal ions are ~4 Å apart [9].

In comparison, in PSII, assembly of the tetra-nuclear manganese cluster at the water-oxidising complex (WOC) is a light-dependent process, called photo-activation. It is best described using the "two-quantum model" [44], according to which a single Mn^{II} ion binds to a high affinity site at the apo-PSII complex and is subsequently photo-oxidised to Mn^{III}, releasing a proton. This is followed by light- independent incorporation of a Ca^{II} ion which induces conformational changes to the complex, making it more stable and to which a second Mn^{II} binds. This Mn^{II}–Mn^{III}–O–Ca^{II} intermediate cluster has been proposed to be stabilised by a μ-oxo bridge until the assembly of the tetra-nuclear Mn_4O_5Ca cluster [45,46].

4.3. Light induced electron transfer in the modified BFR

Photo-active behaviour of the engineered apo-BFR protein scaffold reconstituted with $ZnCe_6$ was investigated using EPR spectroscopy. Upon illumination at 250 K and observing under non-saturating microwave power conditions, a narrow ~6.5 G wide radical cation EPR spectrum centred at $\sim g = 2.0023$ was observed, which was assigned to the oxidised $ZnCe_6^{\bullet+}$ species (Fig. 9a). The line-shape of this spectrum is consistent with that of light-activated $ZnCe_6$ bound to other peptide complexes, reported elsewhere [19,20].

The photo-oxidation of $ZnCe_6$ to a cationic species was observed in the absence of added electron acceptors. This poses an intriguing question about the location of the 'lost' electron during $ZnCe_6^{\bullet+}$ formation. Under the EPR experimental conditions used here, the location of this electron remains unresolved. However, it may be proposed that the $ZnCe_6^{\bullet+}$ species loses the electron to non-specific sites in the buffer (solvated) or within the protein matrix, which either results in loss of the paramagnetic nature of the free electron or the EPR spectrum is too broad to be readily detected above baseline.

Modified BFR assembled with Mn^{II} at the di-nuclear binding site and $ZnCe_6$ at the dimer interface, when illuminated at 295 K yields significantly reduced levels of oxidised $ZnCe_6^{\bullet+}$ species and reveals a ~24 G wide EPR spectrum centred at $\sim g = 2.0048$ that forms 90% of the total observed radical intensity (Fig. 10). This spectrum was assigned to oxidised tyrosine species where the radical most likely originates from a neutral deprotonated tyrosyl form owing to high ~*g*-value [47]. Similar spectral features have been observed for oxidised tyrosine species in engineered bacterial reaction centres [48]. The line-shape observed here is somewhat comparable to the $Y_D^{\bullet}$ and the $Y_Z^{\bullet}$ radical EPR spectra of light-activated PSII, which are centred at $\sim g = 2.0046$ [49,50].

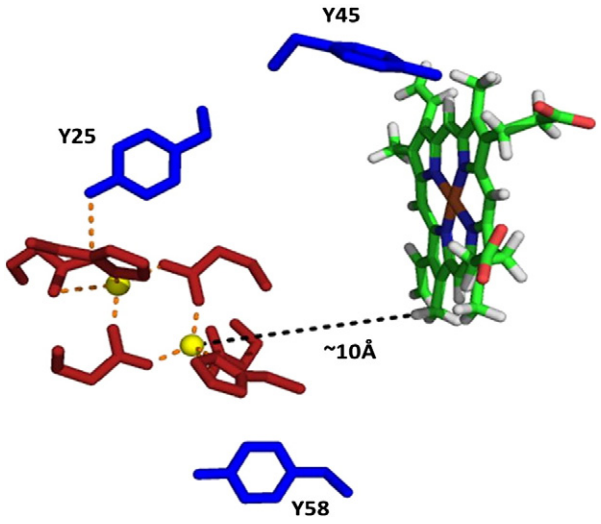

Fig. 12. Placement of the metal centre, proximal tyrosine residues and $ZnCe_6$ in BFR. The three tyrosine residues that are within electron tunnelling distance ~ (<16 Å) of $ZnCe_6$ and nearest metal ion (blue), direct ligands to the metal ions (yellow), edge-to-edge distance (~10 Å) between the bound metal ion and $ZnCe_6$ (black dashes). The bonding network at the metal centre, including the hydrogen bond between Y25 and E94 (orange dashes) is shown.

The $Mn_2^{II,II}$ bound at the di-nuclear site, which is ~10 Å (edge-to-edge) distant from the bound $ZnCe_6$, has significant paramagnetic effects on the saturation behaviour of the oxidised $ZnCe_6^{\bullet+}$ radical species (Fig. 12). The $P^{1/2}$ value of the latter increases from 1.8 (±0.1) μW, in the absence of Mn^{II}, to 15 (±2.2) μW in the presence of Mn^{II}. This change is likely due to the close proximity of the Mn^{II} paramagnetic centre which acts as a relaxation enhancer [51,52]. The half saturation powers of the photo-oxidised $Y^{\bullet}$ species could not be resolved as this radical did not show saturation within the power interval tested for the illuminated BFR^1-Z (+Mn) complex. The $Y_D^{\bullet}$ radical in the Mn-depleted photo-activated PSII samples has been shown to have a $P^{1/2}$ value of ~40–50 μW at 25 K [53]. This close *qualitative* consistency of the spin-relaxation behaviour adds confidence in assigning the ~24 G signal observed in the illuminated BFR-Z (+Mn) complex, to oxidised tyrosine species.

Tyrosine photo-oxidation observed in the BFR^1-Z (+Mn) complex in the presence of bound Mn^{II} can be explained by a 'hole-propagation' mechanism from the oxidised $ZnCe_6^{\bullet+}$ to proximal tyrosine residue(s), generating $Y^{\bullet}$ radical species. This proposition is supported by the observed EPR spectrum of the illuminated BFR^1-Z (+Mn) complex, where the spectrum is composed of ~90% oxidised $Y^{\bullet}$ species and the $ZnCe_6^{\bullet+}$ radical is significantly reduced (Fig. 10 and Table 4).

As has been indicated earlier, in order to examine possible electron transfer pathways by which the $ZnCe_6^{\bullet+}$ is reduced in the engineered BFR, three proximal tyrosine residues (Y25, Y58 and Y45) were mutated to phenylalanine residues. Fig. 12 shows the placement of each with respect to the metal-centre and the photoactive $ZnCe_6$. It was expected that site-specific inactivation of the tyrosine residues will give a direct insight into the photochemical pathways of tyrosine oxidation in BFR through EPR spectroscopy. All three tyrosine variants generated EPR spectra with varying line-widths and spectral features, suggesting that the mutations have some (light-induced) effect on the total paramagnetic nature of the fully assembled engineered BFR, particularly when compared to the BFR^1 complex which was used as the negative control (Fig. 11).

In all cases the radical region spectra revealed a ~20–24 G wide underlying component, after subtraction of scaled amounts of oxidised $ZnCe_6^{\bullet+}$ species (Table 5). This broader component has been assigned to arise from oxidised tyrosine species, due to the line-width and centre *g*-values, found to be 2.0042, 2.0044 and 2.0038 for Y25F, Y58F and Y45F variants respectively. The observed differences in the estimated *g*-values for each of the tyrosine variant likely arise from the small differences associated with estimating the centre field (zero crossing point). The tyrosine radical EPR spectrum obtained for each of the three BFR tyrosine variants could not be readily simulated with single sets of proton hyperfine parameters, as is the case for the highly resolved and well-characterised tyrosine radicals $Y_D^{\bullet}$ and $Y_Z^{\bullet}$ in PSII, or tyrosine radicals from other redox-active systems [47,50,54]. These preliminary EPR simulations were inconsistent with a single isolated tyrosine radical species being present in each case. We thus propose that the ~20–24 G wide radical signal observed in the tyrosine variants upon illumination is possibly a mixed species of more than one oxidised tyrosine radical. Alternatively (or additionally), significant mosaic spread in the tyrosyl methylene carbon/phenyl ring dihedral angle could be present. This would lead to similar effects as the above because the methylene dihedral is important in determining the proton hyperfine structure of the radical signal [55].

Elucidation of the light-induced electron-transfer pathway in the tyrosine variants is further complicated by the varying metal binding affinity and stoichiometry of coupled Mn estimated for each BFR variant using ITC and EPR (Table 7). Tyrosine form Y45F reduced the total yield of the putative $Y^{\bullet}$ radical species by about 36% relative to BFR[1] (in which all tyrosine residues were active). In contrast, the measured spin counts in Y25F and Y58F were only reduced by about 5–6% relative to BFR[1] (Table 7). This result implies that Y45 is a direct donor to the $ZnCe_6^{\bullet+}$ species; and this inference agrees well with the estimated number of reaction centres that are occupied with the coupled di-nuclear metal. In Y45F, the total centres with $Mn_2^{II,II}$ bound to the di-nuclear site are 35% less than in BFR[1], presenting a near-direct correlation between the 'amount' of $Mn_2^{II,II}$ bound to the 'amount' of observed oxidised $Y^{\bullet}$ species. The same correlation was found in the BFR Y25F form, where the estimated centres with bound $Mn_2^{II,II}$ was 5% less than BFR[1] and yield of $Y^{\bullet}$ was reduced by 6% (Table 7). However, this correlation was not observed in the Y58F variant, where it was noted that there are 30% less centres with occupied $Mn_2^{II,II}$, but the total yield of the tyrosine radical is reduced only by 5% compared to BFR[1]. These results, firstly confirm that no tyrosine oxidation is seen (dark or illuminated) in the absence of Mn^{II}. Secondly, that in the presence of Mn^{II} most (≥85 %) tyrosine species is oxidised, *even though* no more than 50% of centres show coupled Mn^{II} (signals from uncoupled monomeric Mn and free Mn were subtracted in Figs. 7 and 8). It is quite possible that Mn sites, such as those here, can show apparently 'isolated' Mn^{II} spectra (i.e. the six hyperfine line species as in Supplementary Fig. C) even if the two Mn^{II} are present, within ~4 Å of each other. This is because the exchange coupling, which is always small, is quite sensitive to the inter-nuclear separation and may be zero or slightly positive even (within the above geometric constraints) with appropriate local structural perturbation [31].

Assuming that the $ZnCe_6^{\bullet+}$ is not reduced by long-range electron transfer from any of the five other tyrosine residues in this system that are ~16–28 Å away from the metal centre, these findings indicate that Y45 is singly the most important residue in the engineered photo-catalytic BFR system. Mutation of Y45 affects both metal binding and forward electron transfer to the oxidised $ZnCe_6^{\bullet+}$. This is supported by the X- ray crystal structure of the Y45F form (Fig. 4). The structure reveals that the conformational change induced is predominantly on the orientation of Y25, which in native *E. coli* BFR is hydrogen bonded to a glutamate residue (E94) that provides a direct ligand for metal binding.

In Y45F, 54% of the $Y^{\bullet}$ is still observed, likely coming from the other two tyrosine residues (Y25 and Y58) (Table 7). The exact mechanism is unclear, however it can be suggested that inactivation of either Y25 or Y58 is compensated by the presence of the other, where the electrons choose the next best option for propagation to the $ZnCe_6^{\bullet+}$, most likely via Tyr45. In the Y58F form, only 25% of the Mn present are coupled, with little effect on the total $Y^{\bullet}$ yield. This suggests that whilst tyrosine is not oxidised in the absence of bound Mn^{II}, the bound metal does not have to be coupled, it may be monomeric uncoupled.

The observation that Y25 and Y58 are redox-active in the BFR reaction centre is an important finding with regards to tyrosine residues as redox-active cofactors in engineered photo-catalytic proteins. Particularly, when compared to the PSII core, where two tyrosine residues (Y_Z, Y_D) are photo-oxidised by P_{680}^{+} but only Y_Z is essential for oxygen evolution (reviewed in [47,55]).

Here, we propose that around half (~54%) of the oxidised $Y^{\bullet}$ species is a combination of Y25 and Y58, where mutation of one is compensated by the presence of the other. However, Y45, which is in van der Waals contact with the photoactive $ZnCe_6$ (Fig. 12), is singly most important for light-induced electron propagation, functioning in sequence with either Y25 and Y58 both, or one of the two depending on availability. In the BFR[1] system, where all three tyrosine residues are present, the question remains as to which of Y25 or Y58 is the preferred electron donor upon illumination. Further investigation will be needed to answer this. From comparisons of the spin-counts and spectral shapes of the oxidised $Y^{\bullet}$ in the Y25F and Y58F variants, it can be suggested that both are equally redox-active.

Table 7
A summary table to deduce the light-induced electron path in BFR variants, where BFR[1] is opted as a −ve control. The electron acceptor is unresolved (see Section 4.3). The metal binding is defined strong or weak relative to the BFR[1] form.

BFR mutant	active metal centre	active tyrosine	$ZnCe_6$	e- acceptor
BFR[1] - Z	none bound	none		
BFR[1] (- control)	Mn^{II} - Mn^{II}	Y25 Y58 Y45		
ITC:	strong binding			
EPR:	55% bound	$Y^{\bullet}$ = 90 %		
Y25F	Mn^{II} - Mn^{II}	Y58 Y45		
ITC:	strong binding			
EPR:	50% bound	$Y^{\bullet}$ = 84 %	→ $ZnCe_6^{\bullet+}$ →	?
Y58F	Mn^{II} - Mn^{II}	Y25 Y45		
ITC:	binding affinity n.d.			
EPR:	25% bound	$Y^{\bullet}$ = 85 %		
Y45F	Mn^{II} - Mn^{II}	Y25 Y58		
ITC:	weak binding			
EPR:	20% bound	$Y^{\bullet}$ = 54 %		

4.4. Electron transfer in BFR reaction centre

There was no direct evidence in this research for an alternative pathway involving the photo-oxidation sequence—that is, the Mn ions are directly oxidised by the chlorin, and in turn the tyrosine is oxidised by the Mn ions. This pathway might be explored if the oxidation potentials were better understood in the system. This is very challenging partly because there are a number of tyrosine residues and the oxidation potentials of tyrosine are not readily accessed with redox titration directly [34].

Here we report the oxidation potential of $ZnCe_6$ in aqueous buffer, pH 10 (unbound to the BFR- RC in the absence of Mn ions) to be at 0.583 V, as measured using cyclic voltammetry (Supplementary Fig. D). The oxidation of $ZnCe_6$ appears to be quasi-reversible with a corresponding reduction wave at 0.496 V. The observed oxidation potential of $ZnCe_6$ is slightly lower than tyrosine residues which typically oxidises at potentials above 0.6 V within redox proteins [34,56]. It is notable that the light-induced electron hole migration within the BFR matrix seen here is not observed in the absence of Mn ions. Evidently these do not have to be coupled (but might be singly located) at the di-nuclear

metal centre. Ligation of Mn^{II} to BFR could either; (a) alter the redox potential of $ZnCe_6$, making it more oxidising, (b) alter the redox potential of the tyrosine residues or (c) the redox potential of both the $ZnCe_6$ and the redox-active tyrosine residue(s) are varied to different degrees. The fact that Mn^{II} bound 'uncoupled' (at the di-nuclear site or elsewhere) appears to be the minimal requirement for (any) tyrosine oxidation, suggests that option (a) is the most likely and has the virtue of a simple electrostatic explanation.

One study has estimated the redox potential of $ZnCe_6$ in the BFR-RC to be 0.54 V using DFT calculations, where E_m of $ZnCe_6$ in DMSO has been used a reference [57]. We do not find the experimental evidence provided in [57] convincing mainly due to the unexplained peaks in the cyclic voltammetry data, the lack of references to support the two electron oxidation argument, as well as significant differences in the methods and solvents used for sample preparation. We recommend further investigation.

5. Concluding remarks

In this paper, a rationally designed *E. coli* BFR homodimer was shown to readily bind a photoactive porphyrin $ZnCe_6$ within the intrinsically hydrophobic pocket at the dimer interface, together with a magnetically coupled $Mn_2^{II,II}$ pair at the di-nuclear metal binding site. Light-induced experiments of the BFR-complex in the absence of bound Mn^{II} revealed photo-oxidation of the $ZnCe_6$ to a cationic $ZnCe_6^{\bullet+}$ radical species, which was reduced via tyrosine oxidation in the presence of bound Mn^{II}. Three site-specific tyrosine variants (Y25F, Y58F and Y45F) were investigated to discern the location and paramagnetic characteristics of the oxidised $Y^{\bullet}$ species in this engineered system. Thorough analysis of the available experimental evidence suggested that the $ZnCe_6^{\bullet+}$ is unlikely to be reduced by a single isolated tyrosine residue in the photo-catalytic BFR. It is proposed that the proximal Y45 (~3.1 Å) is especially important for generating the photo-oxidised tyrosine species in this system, as well as for binding of the exchange coupled Mn^{II}–Mn^{II} at the di-nuclear site. The electron–hole propagation pathway has been shown to also involve Y25 and Y58, where the absence of one can be compensated by the presence of the other. In all cases however, it is clear that tyrosine oxidation by the pigment is dependent on Mn^{II} ligation (either singly or doubly bound) at the metal binding sites of BFR.

Supplementary data to this article can be found online at http://dx.doi.org/10.1016/j.bbabio.2014.07.019.

Acknowledgements

KH was supported by an ANU Postgraduate Scholarship. Support for this work was provided by the Australian Research Council FT0990972. JWM was supported by a BBSRC David Phillips Fellowship (BB/F023308/1).We thank Diamond Light Source for access to the beamlines that contributed to the results presented here.

References

[1] W. Hillier, G.T. Babcock, Photosynthetic reaction centers, Plant Physiol. 125 (2001) 33–37.
[2] M.F. Hohmann-Marriott, R.E. Blankenship, Evolution of photosynthesis, Annu. Rev. Plant Biol. 62 (2011) 515–548.
[3] B. Conlan, Designing photosystem II: Molecular engineering of photo-catalytic proteins, Photosynth. Res. 98 (2008) 687–700.
[4] K. Hingorani, W. Hillier, Perspectives for photobiology in molecular solar fuels, Aust. J. Chem. 65 (2012) 643–651.
[5] J. Murray, Chapter 14 Redox active protein maquettes: multi-functional "green enzymes", Molecular Solar Fuels, The Royal Society of Chemistry, 2012.
[6] B. Conlan, N. Cox, J.-H. Su, W. Hillier, J. Messinger, W. Lubitz, P.L. Dutton, T. Wydrzynski, Photo-catalytic oxidation of a di-nuclear manganese centre in an engineered bacterioferritin 'reaction centre', Biochim. Biophys. Acta 1787 (2009) 1112–1121.
[7] J. Yariv, A.J. Kalb, R. Sperling, E.R. Bauminger, S.G. Cohen, S. Ofer, The composition and the structure of bacterioferritin of *Escherichia coli*, Biochem. J. 197 (1981) 171–175.
[8] J.M.A. Smith, G.C. Ford, P.M. Harrison, J. Yariv, A.J. Kalb, Molecular size and symmetry of the bacterioferritin of *Escherichia coli*: X-ray crystallographic characterization of four crystal forms, J. Mol. Biol. 205 (1989) 465–467.
[9] F. Frolow, A.J. Kalb, J. Yariv, Structure of a unique twofold symmetrical heme-binding site, Nat. Struct. Biol. 1 (1994) 453–460.
[10] A. Dautant, J.B. Meyer, J. Yariv, G. Precigoux, R.M. Sweet, A.J. Kalb, F. Frolow, Structure of a monoclinic crystal form of cytochrome *b*1 (bacterioferritin) from *E. coli*, Acta Crystallogr. D Biol. Crystallogr. 54 (1998) 16–24.
[11] K. Hingorani, B. Conlan, W. Hillier, T. Wydrzynski, Elucidating photochemical pathways of tyrosine oxidation in an engineered bacterioferritin 'reaction centre', Aust. J. Chem. 62 (2009) 1351–1354.
[12] F.W.J. Teale, Cleavage of the haem-protein link by acid methylethylketone, Biochim. Biophys. Acta 35 (1959) (543-543).
[13] B.A. Barry, G.T. Babcock, Tyrosine radicals are involved in the photosynthetic oxygen-evolving system, Proc. Natl. Acad. Sci. U. S. A. 84 (1987) 7099–7103.
[14] C.W. Hoganson, M. Sahlin, B.M. Sjoberg, G.T. Babcock, Electron magnetic resonance of the tyrosyl radical in ribonucleotide reductase from *Escherichia coli*, J. Am. Chem. Soc. 118 (1996) 4672–4679.
[15] N.E. Le Brun, A. Crow, M.E.P. Murphy, A.G. Mauk, G.R. Moore, Iron core mineralisation in prokaryotic ferritins, Biochim. Biophys. Acta 1800 (2010) 732–744.
[16] R.J. Debus, B.A. Barry, G.T. Babcock, L. McIntosh, Site-directed mutagenesis identifies a tyrosine radical involved in the photosynthetic oxygen-evolving system, Proc. Natl. Acad. Sci. U. S. A. 85 (1988) 427–430.
[17] G.H. Noren, R.J. Boerner, B.A. Barry, EPR characterization of an oxygen-evolving photosystem II preparation from the transformable cyanobacterium *Synechocystis* 6803, Biochemistry 30 (1991) 3943–3950.
[18] R.J. Boerner, K.A. Bixby, A.P. Nguyen, G.H. Noren, R.J. Debus, B.A. Barry, Removal of stable tyrosine radical D^+ affects the structure or redox properties of tyrosine Z in manganese-depleted photosystem II particles from *Synechocystis* 6803, J. Biol. Chem. 268 (1993) 1817–1823.
[19] A.R. Razeghifard, T. Wydrzynski, Binding of Zn-chlorin to a synthetic four-helix undle peptide through histidine ligation, Biochemistry 42 (2003) 1024–1030.
[20] S. Hay, B.B. Wallace, T.A. Smith, K.P. Ghiggino, T. Wydrzynski, Protein engineering of cytochrome b_{562} for quinone binding and light-induced electron transfer, Proc. Natl. Acad. Sci. U. S. A. 101 (2004) 17675–17680.
[21] R.T. Baker, Protein expression using ubiquitin fusion and cleavage, Curr. Opin. Biotechnol. 7 (1996) 541–546.
[22] A.M. Catanzariti, T.A. Soboleva, D.A. Jans, P.G. Board, R.T. Baker, An efficient system for high-level expression and easy purification of authentic recombinant proteins, Protein Sci. 13 (2004) 1331–1339.
[23] E.R. Bauminger, P.M. Harrison, D. Hechel, I. Nowik, A. Treffry, Mossbauer spectroscopic investigation of structure–function relations in ferritins, Biochim. Biophys. Acta 1118 (1991) 48–58.
[24] A. Mennenga, W. Gartner, W. Lubitz, H. Gorner, Effects of noncovalently bound quinones on the ground and triplet states of zinc chlorins in solution and bound to de novo synthesized peptides, PCCP 8 (2006) 5444–5453.
[25] J. Newman, D. Egan, T.S. Walter, R. Meged, I. Berry, M. Ben Jelloul, J.L. Sussman, D.I. Stuart, A. Perrakis, Towards rationalization of crystallization screening for small- to medium-sized academic laboratories: the PACT/JCSG+ strategy, Acta Crystallogr. D 61 (2005) 1426–1431.
[26] W. Kabsch, XDS, Acta Crystallogr. D 66 (2010) 125–132.
[27] G. Winter, C.M.C. Lobley, S.M. Prince, Decision making in xia2, Acta Crystallogr. D 69 (2013) 1260–1273.
[28] A.J. McCoy, R.W. Grosse-Kunstleve, P.D. Adams, M.D. Winn, L.C. Storoni, R.J. Read, Phaser crystallographic software, J. Appl. Crystallogr. 40 (2007) 658–674.
[29] P. Emsley, B. Lohkamp, W.G. Scott, K. Cowtan, Features and development of Coot, Acta Crystallogr. Sect. D: Biol. Crystallogr. 66 (2010) 486–501.
[30] G.N. Murshudov, P. Skubak, A.A. Lebedev, N.S. Pannu, R.A. Steiner, R.A. Nicholls, M.D. Winn, F. Long, A.A. Vagin, REFMAC5 for the refinement of macromolecular crystal structures, Acta Crystallogr. D 67 (2011) 355–367.
[31] S.V. Khangulov, P.J. Pessiki, V.V. Barynin, D.E. Ash, G.C. Dismukes, Determination of the metal ion separation and energies of the three lowest electronic states of dimanganese(II, II) complexes and enzymes: catalase and liver arginase, Biochemistry 34 (1995) 2015–2025.
[32] B.S. Antharavally, R.R. Poyner, P.W. Ludden, EPR spectral evidence for a binuclear Mn(II) center in dinitrogenase reductase-activating glycohydrolase from *Rhodospirillum rubrum*, J. Am. Chem. Soc. 120 (1998) 8897–8898.
[33] S. Macedo, C.V. Romao, E. Mitchell, P.M. Matias, M.Y. Liu, A.V. Xavier, J. LeGall, M. Teixeira, P. Lindley, M.A. Carrondo, The nature of the di-iron site in the bacterioferritin from *Desulfovibrio Desulfuricans*, Nat. Struct. Biol. 10 (2003) 285–290.
[34] A. Harriman, Further comments on the redox potentials of tryptophan and tyrosine, J. Phys. Chem. 91 (1987) 6102–6104.
[35] A. van Eerde, S. Wolternik-van Loo, J. van der Oost, B.W. Dijkstra, Fortuitous structure determination of 'as-isolated' *Escherichia coli* bacterioferritin in a novel crystal form, Acta Crystallogr. Sect. F: Struct. Biol. Cryst. Commun. 62 (2006) 1061–1066.
[36] M. Nappa, J.S. Valentine, The influence of axial ligands on metalloporphyrin visible absorption spectra. Complexes of tetraphenylporphinatozinc, J. Am. Chem. Soc. 100 (1978) 5075–5080.
[37] S.C. Andrews, N.E. Lebrun, V. Barynin, A.J. Thomson, G.R. Moore, J.R. Guest, P.M. Harrison, Site-directed replacement of the coaxial heme ligands of bacterioferritin generates heme-free variants, J. Biol. Chem. 270 (1995) 23268–23274.
[38] A.M. Keech, N.E. LeBrun, M.T. Wilson, S.C. Andrews, G.R. Moore, A.J. Thomson, Spectroscopic studies of cobalt(II) binding to *Escherichia coli* bacterioferritin, J. Biol. Chem. 272 (1997) 422–429.

[39] N.E. Le Brun, A.M. Keech, M.R. Mauk, A.G. Mauk, S.C. Andrews, A.J. Thomson, G.R. Moore, Charge compensated binding of divalent metals to bacterioferritin: H^+ release associated with cobalt(II) and zinc(II) binding at dinuclear metal sites, FEBS Lett. 397 (1996) 159–163.
[40] D.E. Wilcox, Isothermal titration calorimetry of metal ions binding to proteins: an overview of recent studies, Inorg. Chim. Acta 361 (2008) 857–867.
[41] S. Baaghil, A.J. Thomson, G.R. Moore, N.E. Le Brun, Studies of copper(II)-binding to bacterioferritin and its effect on iron(II) oxidation, Dalton Trans. (2002) 811–818.
[42] G.H. Reed, G.D. Markham, EPR of Mn(II) complexes with enzymes and other proteins, Biol. Magn. Reson. (1984) 73–142.
[43] D.E. DeVos, B.M. Weckhuysen, T. Bein, ESR fine structure of manganese ions in zeoliteA detects strong variations of the coordination environment, J. Am. Chem. Soc. 118 (1996) 9615–9622.
[44] G.M. Cheniae, I.F. Martin, Effects of hydroxylamine on photosystem II 1. Factors affecting decay of O_2 evolution, Plant Physiol. 47 (1971) 568.
[45] J. Dasgupta, G.M. Ananyev, G.C. Dismukes, Photoassembly of the water-oxidizing complex in photosystem II, Coord. Chem. Rev. 252 (2008) 347–360.
[46] K. Becker, K.U. Cormann, M.M. Nowaczyk, Assembly of the water-oxidizing complex in photosystem II, J. Photochem. Photobiol. 104 (2011) 204–211.
[47] S. Styring, J. Sjoholm, F. Mamedov, Two tyrosines that changed the world: interfacing the oxidizing power of photochemistry to water splitting in photosystem II, Biochim. Biophys. Acta 1817 (2012) 76–87.
[48] L. Kalman, R. LoBrutto, J.P. Allen, J.C. Williams, Modified reaction centres oxidize tyrosine in reactions that mirror photosystem II, Nature 402 (1999) 696–699.
[49] D.A. Berthold, G.T. Babcock, C.F. Yocum, A highly resolved, oxygen-evolving photosystem II preparation from spinach thylakoid membranes-electron-paramagnetic-res and electron-transport properties, FEBS Lett. 134 (1981) 231–234.
[50] C.L. Ma, B.A. Barry, Electron paramagnetic resonance characterization of tyrosine radical, M^+, in site-directed mutants of photosystem II (t), Biophys. J. 71 (1996) 1961–1972.
[51] D.J. Hirsh, W.F. Beck, J.B. Innes, G.W. Brudvig, Using saturation recovery EPR to measure distances in proteins: applications to photosystem II, Biochemistry 31 (1992) 532–541.
[52] D. Koulougliotis, J.B. Innes, G.W. Brudvig, Location of chlorophyll (Z) in photosystem II, Biochemistry 33 (1994) 11814–11822.
[53] S. Styring, A.W. Rutherford, In the oxygen-evolving complex of photosystem II the S0 state is oxidized to the S1 state by D^+ (signal II slow), Biochemistry 26 (1987) 2401–2405.
[54] C.W. Hoganson, C. Tommos, The function and characteristics of tyrosyl radical cofactors, Biochim. Biophys. Acta 1655 (2004) 116–122.
[55] B.A. Barry, Proton coupled electron transfer and redox active tyrosines in photosystem II, J. Photochem. Photobiol. B Biol. 104 (2011) 60–71.
[56] J.J. Warren, J.R. Winkler, H.B. Gray, Redox properties of tyrosine and related molecules, FEBS Lett. 586 (2012) 596–602.
[57] A. Mahboob, S. Vassiliev, P.K. Poddutoori, A. van der Est, D. Bruce, Factors controlling the redox potential of ZnCe6 in an engineered bacterioferritin photochemical 'reaction centre', PLoS One 8 (2013).